



Laboratory Simulation of the Positron–Dust Interaction and its Implication for Interstellar Dark Clouds

Jan Wild¹, Jakub Čížek¹, Libor Nouzák¹, Jiří Pavlů¹, Jana Šafránková¹, Zdeněk Němeček¹, Jakub Vaverka¹, Dalibor Nosek¹, Tomáš Burian^{2,3}, Anna Wildová⁴, and Jan Broulím⁵

¹ Charles University, Faculty of Mathematics and Physics V Holešovičkách 2, 180 00 Prague, Czech Republic; jan.wild@mff.cuni.cz

² Institute of Physics of the Czech Academy of Sciences Na Slovance 1999/2, 182 21 Prague, Czech Republic

³ Institute of Plasma Physics of the Czech Academy of Sciences Za Slovankou 1782/3, 182 00 Prague, Czech Republic

⁴ Czech University of Life Sciences in Prague, Faculty of Tropical AgriSciences Kamýcká 961/129, 165 00 Prague, Czech Republic

⁵ Czech Technical University, Institute of Technical and Experimental Physics, Husova 240/5, 110 00 Prague, Czech Republic

Received 2022 February 3; revised 2022 October 31; accepted 2022 November 2; published 2023 January 6

Abstract

We report the first laboratory experiment dealing with the interaction of a cosmic dust simulant with positrons emitted from a ²²Na radioisotope. Measurements of a charge of micrometer SiO₂ dust grains with an accuracy of one elementary charge e revealed $+1 e$ steps due to positron annihilation inside the grain. The observed average rate of these charging events agrees well with prediction of a model based on the continuous slowing down approximation of energetic of positrons inside the grain. Less frequent charge steps larger than $+1 e$ were attributed to emission of secondary electrons during positron slowing down. The determined coefficient of secondary electron emission is approximately inversely proportional to the grain radius. The experimental results led us to the formulation of a possible scenario of interstellar dark clouds charging.

Unified Astronomy Thesaurus concepts: [Interstellar dust \(836\)](#); [Laboratory astrophysics \(2004\)](#); [Nuclear physics \(2077\)](#); [Interdisciplinary astronomy \(804\)](#)

1. Introduction

About one percent of the observable matter of the interstellar medium (ISM) is composed of dust, i.e., mesoscopic objects with size in the order of $0.01\text{--}10\ \mu\text{m}$ (Draine 2011). Spectroscopic data show that interstellar dust grains consist mainly of carbon compounds and silicates (Draine 2003).

The dust grains cluster into large interstellar clouds that may develop into new stars or planetary systems in the future (van Dishoeck 2014). There is a variety of mechanisms that can electrically charge cosmic dust grains: the capture of ambient electrons and ions, secondary electron emission induced by energetic electron and ion impacts, photoemission due to ultraviolet (UV) electromagnetic radiation, field emission of electrons, triboelectric effects, and field evaporation of ions. The electrostatic force resulting from charging/discharging of the interstellar dust grains by the interaction with photons and charged particles of cosmic radiation (CR) is an important process for a dust cloud evolution. The UV photoemission charging is broadly studied and leads to charging of grains to low positive potentials (e.g., Nouzák et al. 2016), and thus we concentrate on the charging by massive particles.

Electron charging (Adriani et al. 2015) of dust grains has been studied in laboratories and modeled using computer simulations in the past (e.g., Svestka et al. 1993; Renoud et al. 2004; Richterová et al. 2006). One of the most important features of mesoscopic objects with highly curved surfaces (dust grains) is that the electron–electron secondary emission coefficient is significantly higher compared to planar surfaces (Pavlů et al. 2009; Richterová et al. 2010). On the other hand, a proton (Adriani et al. 2013a) or, more generally, the ion

component of CR is not too important in this regard because the ion-induced electron emission is rather ineffective (Jerab et al. 2007; Pavlu et al. 2008). However, the ISM also contains positrons in addition to protons and electrons (Padovani et al. 2020).

Positrons are emitted by β^+ radioisotopes, which are produced in massive star cores (²⁶Al) or in novae (²²Na) and supernovae explosions (⁴⁴Ti, ⁵⁶Ni). The most important astrophysical β^+ positron emitters are the low- Z long-lived radioisotopes ²²Na, ²⁶Al, ⁴⁴Ti, and ⁵⁶Ni (Prantzos et al. 2011). The lifetimes of these radioisotopes are long enough so that positrons can escape from the novae or supernovae envelopes (Guessoum et al. 2006). These β^+ radioisotopes produce positrons with a continuous energy spectrum characterized by a mean energy of a few hundreds of keV and an end-point energy in the order of MeV. In addition, positrons are created by pair production in the hot accretion disk around black holes or neutron stars (Prantzos et al. 2011). Positrons with high enough energies are able to escape to the ISM. High-energy positrons in CR are produced by inelastic interaction of relativistic protons with interstellar gas, which produces neutral and charged pions and kaons. Decay of positively charged pions produces positrons via the decay channel $\pi^+ \rightarrow \mu^+ \nu_\mu$, $\mu^+ \rightarrow \bar{\nu}_\mu \nu_e e^+$. Positively charged kaons decay to muons $K^+ \rightarrow \mu^+ \nu_\mu$ (63.5%) or to pions $K^+ \rightarrow \pi^0 \pi^+$ (21.2%) whose decays represent additional sources of positrons in CR (Strong et al. 2007). Hence, one can conclude that positrons represent an important component of CR.

Voyager 1 probed the energy spectrum of CR, and the data revealed that at energies below ~ 100 MeV the electron and positron contribution in CR dominates and exceeds significantly the contribution of protons (Cummings et al. 2016). Note that the Cosmic Ray Subsystem telescopes of Voyager 1 could not distinguish between electrons and positrons, so both electrons and positrons detected by Voyager 1 are referred to as

electrons. Nevertheless, the data obtained by Voyager 1 (Cummings et al. 2016) in combination with the PAMELA (Adriani et al. 2013b) spacecraft and Monte Carlo simulations (Strong et al. 2011) suggest that tens of electrons and positrons fall on a spherical dust grain of diameter $1 \mu\text{m}$ in the interstellar space per year; from this amount, the fraction of positrons is approximately 5%–20% (Ackermann et al. 2012; Aguilar et al. 2013).

Positrons in the ISM lose their energy by excitation and ionization of gas atoms and molecules, predominantly H_2 , H, and He in interstellar dark clouds (IDCs). In addition, positrons slow down by the interaction with mesoscopic dust grains contained in IDCs (Zurek 1985). When a positron is thermalized inside a dust grain it is annihilated there with a high probability. Moreover, a pair of a positron and electron can be created due to the interaction of energetic gamma rays (energies higher than 1022 keV) with dust grains. Due to these reasons, the impact of positrons on dust is a relevant question requiring further examination.

Since positrons can serve, for example, as probes of open volume lattice defects, the interaction of positrons with bulk solids (Krause-Rehberg & Leipner 1999) and solid surfaces has been intensively studied; see, e.g., reviews by Schultz & Lynn (1988) and Hugenschmidt (2016), and references therein. Positron scattering on single atoms (Charlton 1985) and molecules (Brunger et al. 2017) has been also investigated experimentally, but the interplay between positrons and objects of mesoscopic sizes has been a subject of computer simulations only (Guessoum et al. 2006; Fuller et al. 2019).

This paper presents results of laboratory experiments in which cosmic dust simulants caught in an electrodynamic quadrupole trap were bombarded by positrons emitted by a ^{22}Na radioisotope, with the motivation to study the charging of dust grains due to their interaction with positrons. The results of laboratory measurements are compared with standard models of positron interaction with matter. This comparison suggests that a dominant portion of charging events is caused by positron annihilation inside the grain. We have also found that the electron emission leading to additional grain charging increases with decreasing diameter of the grain. These processes would contribute to positive charging of the outer layer of IDCs, as will be shown in the following text.

2. Experimental Setup

We selected a collection of spherically shaped SiO_2 grains with diameters ranging from 1 to $3 \mu\text{m}$ as analogues of interstellar dust. A single grain was caught in an electrodynamic quadrupole trap situated inside a vacuum chamber with a working pressure of less than 10^{-5} Pa (Beránek et al. 2012). The grain oscillation frequency is the only measurable quantity, and we have developed several techniques to determine the grain mass, charge, capacitance, and other parameters (Pavlů et al. 2004). The grain charge-to-mass ratio is computed from its oscillation frequency that is determined from the grain projection onto a position-sensitive detector (Nouzák et al. 2016). The method is sensitive enough to quantify the change of the charge caused by one elementary charge (Žilavý et al. 1999; Pavlů et al. 2004) and it allows us to estimate also the mass of a trapped grain. The parameters—the grain mass, its diameter, and the density of SiO_2 glass—of investigated grains are summarized in Table 1 together with the results of our experiments, which will be discussed later. The

grains are denoted as G_1 – G_4 , and they come from two different manufacturers: G_1 was produced by Palas Karlsruhe and G_2 – G_4 were supplied by microParticles GmbH. This is the reason for the different densities of grains G_1 and G_2 – G_4 .

Trapped grains were bombarded with positrons emitted by a ^{22}Na radioisotope. The positron source, consisting of a $^{22}\text{NaCl}$ salt with an activity of ≈ 5 MBq, was placed in a special container as depicted in Figure 1. The container collimates the flux of emitted positrons into the test space and attenuates gamma radiation generated by β^+ decay and by positron annihilations in container walls. The positron source was covered by a $12 \mu\text{m}$ thick Kapton[®] foil (DuPont) in order to prevent any leakage of ^{22}Na into the vacuum chamber.

3. Modelling of Positron Interaction with Mesoscopic Grains

The energy spectrum of the positrons emitted by a β^+ radioisotope can be expressed using the expression (Leo 1987)

$$N_0(E) = F(Z, E) \sqrt{E^2 + 2Em_0c^2} \cdot (E_{\text{max}} - E)^2 (E + m_0c^2), \quad (1)$$

where E is the kinetic energy of emitted positrons, E_{max} is the end-point energy (maximum energy of emitted positrons), m_0c^2 is the positron rest energy, and $F(Z, E)$ is the Fermi function (Fermi 1934). The energy spectrum $N_0(E)$ of positrons emitted by ^{22}Na is continuous with an average energy $E_{\text{mean}} = 204$ keV and end-point energy $E_{\text{max}} = 545$ keV, and it is plotted in Figure 2 by a green line.

Positrons penetrate first through the Kapton[®] foil, where they lose a part of their kinetic energy mainly by inelastic collisions with electrons and by emission of bremsstrahlung radiation. A total positron stopping power, $S = -dE/dx$, is defined as the average energy loss per unit path length through the matter (Leo 1987) and consists of the collision stopping power, $S_{\text{collision}}$, described by the Bhabha equation (Groom & Klein 2000), and the radiative stopping power, $S_{\text{radiation}}$, which can be determined using the radiation length introduced by Tsai (1974). A simple expression describing the positron stopping power in the energy range below 500 keV (where energy losses by inelastic collisions with electrons are predominant) has been approximated (Gupta et al. 1982; Batra 1987). In this approximation, the total positron stopping power is expressed by a product of two functions; one of them depends on the Z number of the material, and the second one is connected with the positron kinetic energy, E . Within the parameterization by Gupta et al. (1982), the total positron stopping power in a matter is given by the expression

$$S_G(E) = \rho(uZ + w) \frac{\gamma^2}{\gamma^{aZ+b} - 1}, \quad (2)$$

where ρ is the density of the material, $\gamma = (E + m_0c^2)/m_0c^2$, and the constants of a , b , and w are $a = -0.0040$, $b = 1.8496$, and $w = 1.3230 \text{ MeV cm}^2 \text{ g}^{-1}$. The Z -dependent constant u is 0.05458 and $0.02420 \text{ MeV cm}^2 \text{ g}^{-1}$ for the Kapton[®] foil and SiO_2 grain, respectively (Gupta et al. 1982). The energy loss of positrons in the Kapton[®] foil was calculated as

$$\Delta E = \int_0^{x_0} S_G(E) dx, \quad (3)$$

Table 1
Parameters of Investigated Grains G₁–G₄

Grain	Diameter (μm)	Mass (pg)	Density (g cm^{-3})	Duration (day)	N_{tot}^+	N_{tot}^-	τ (hr)	τ^* (hr)	f_{annih}^{-1} (hr)
G ₁	1.07 ± 0.04	1.4 ± 0.2	2.2	68	20	0	70 ± 20	70 ± 20	88
G ₂	1.89 ± 0.05	6.5 ± 0.5	1.85	53	29	4	41 ± 8	35 ± 8	29
G ₃	2.32 ± 0.04	12.1 ± 0.6	1.85	25	20	1	28 ± 6	20 ± 4	16
G ₄	2.83 ± 0.04	21.9 ± 0.1	1.85	50	93	8	12 ± 1	10 ± 1	9

Note. Grain diameter, density of SiO₂ glass, duration of measurements, the total number N_{tot}^+ of detected positive charging events, the total number N_{tot}^- of detected negative charging events, the expected value τ of exponential distribution which is in the best agreement with experimental data, the expected value τ^* corrected for decay of the ²²Na radioisotope, and the mean time interval between annihilation events f_{annih}^{-1} calculated using Equation (5).

where $x_0 = 12 \mu\text{m}$ is the Kapton[®] foil thickness. The cross section for positron annihilation with an electron was derived by Dirac (1930) and it strongly increases with decreasing energy of the positron. As a consequence, positrons are annihilated predominantly in the thermalized state, and we assume that a positron is annihilated when its energy decreases down to ≈ 0.01 eV (Puska & Nieminen 1994). The energy losses were calculated for positrons with initial energies given by the ²²Na β^+ spectrum, $N_0(E)$ (the green curve in Figure 2), and the resulting energy spectrum, $N_1(E)$, of positrons passing through the Kapton[®] foil is plotted in Figure 2 by the blue line.

The probability that a positron emitted by a source hits a grain with diameter d is

$$P_{\text{hit}} = \frac{d^2}{16 l^2}, \quad (4)$$

where $l = 25$ mm is the distance between the ²²NaCl source spot and the grain (Figure 1). Taking the largest grain G₄ as an example, this probability is as small as 8×10^{-10} . Using the energy spectrum $N_1(E)$ of positrons penetrating through the Kapton[®] foil, the energy losses of positrons hitting a grain with diameter d were calculated from Equation (3) under an assumption of a penetration depth $x_0 = \frac{2}{3}d$, that is, the average path traveled by a positron through the spherical grain. Similar to the Kapton[®] foil, it is assumed that the positron is annihilated when the positron energy inside the grain decreases down to ≈ 0.01 eV. The range of positron energies stopped in the grain G₄ is indicated in Figure 2 by the hatched red area. Using an initial activity of the positron source of 5 MBq, the rate of positrons hitting the grain G₄ is $3 \times 10^{-3} \text{ s}^{-1}$.

The mean rate of positron annihilations in the grain captured in the trap can be expressed as

$$f_{\text{annih}} = A P_{\text{hit}} \int_0^{E_{\text{max}}} N_1(E) P_{\text{stop}}(E) dE, \quad (5)$$

where A is the activity of a positron source, $N_1(E)$ is the energy spectrum of the positrons passed through the Kapton[®] foil, and $P_{\text{stop}}(E)$ expresses the probability that a positron with kinetic energy E will be stopped inside the grain. The probability P_{stop} is calculated using the total positron stopping power (Gupta et al. 1982) and the energy loss expressed by Equation (3). When the positron energy inside the grain decreases down to ≈ 0.01 eV, the positron is stopped, $P_{\text{stop}} = 1$. If the positron energy after a passage through the grain is still higher, we set $P_{\text{stop}} = 0$. The majority of positrons passes through the grain

without being annihilated but approximately 0.8% of incident positrons is stopped and annihilated inside grain G₄.

The rate of positron annihilation events, f_{annih} , for grains G₁–G₄ calculated using Equation (5) falls into the range of $(3.2\text{--}30) \times 10^{-6} \text{ s}^{-1}$ and increases with grain size. The inverse of the calculated annihilation rate, f_{annih}^{-1} , representing the expected mean time interval between the annihilation events, is listed in Table 1. Since the probability for positron annihilation inside the grain is a time-independent quantity, the time period between successive annihilation events is a random variable with the exponential distribution.

4. Experimental Study of the Positron–Grain Interaction

In our laboratory simulations, each grain was kept in the linear electrodynamic quadrupole trap (Beránek et al. 2012) for 1–2 months and its charging by the interaction with the positron beam was monitored. Note that measurements were time consuming and took hundreds of hours.

As an example, the record of the first 450 hr of the G₄ grain charging is shown in Figure 3. We actually recorded the grain oscillation frequency, and recalculation into the grain charge is based on a preliminary calibration. The evolution of the grain charge in the course of time shown in the figure uses a relation $q + e \approx f + 0.0165$, where the grain charge, q , is expressed in elementary charges and the oscillation frequency, f , in hertz. One can see two types of grain charge variations. The smooth and small changes, like those observed during first 30 hr of the experiment, are partly caused by drifts of the recording electronics and partly by changes of the temperature in the laboratory leading to changes of the dimensions of the trap, affecting the conversion of the grain oscillation frequency to its charge (Beránek et al. 2012). Above it, one can identify step-like variations of different heights that are caused by charging events. The smallest jumps correspond to one elementary charge, but also multiple charging events are recorded. The heights of the identified events are distinguished by colors. The jumps increasing the grain charge are attributed to positron annihilation and/or to the emission of electron(s) from the grain. There are also three jumps down, all of them with a height corresponding to one elementary charge, that are caused by a capture of a low-energy electron. Such electrons are produced by the secondary emission or photoemission from the trap rods and/or from the chamber’s inner surface. The presence of such electrons cannot be avoided but their number is very small (three events in Figure 3) and we do not consider them in further analysis.

The right-hand scales in Figure 4 show cumulative histograms of detected time intervals, Δt , between observed positive charging events for grains G₁–G₄. Inspection of the

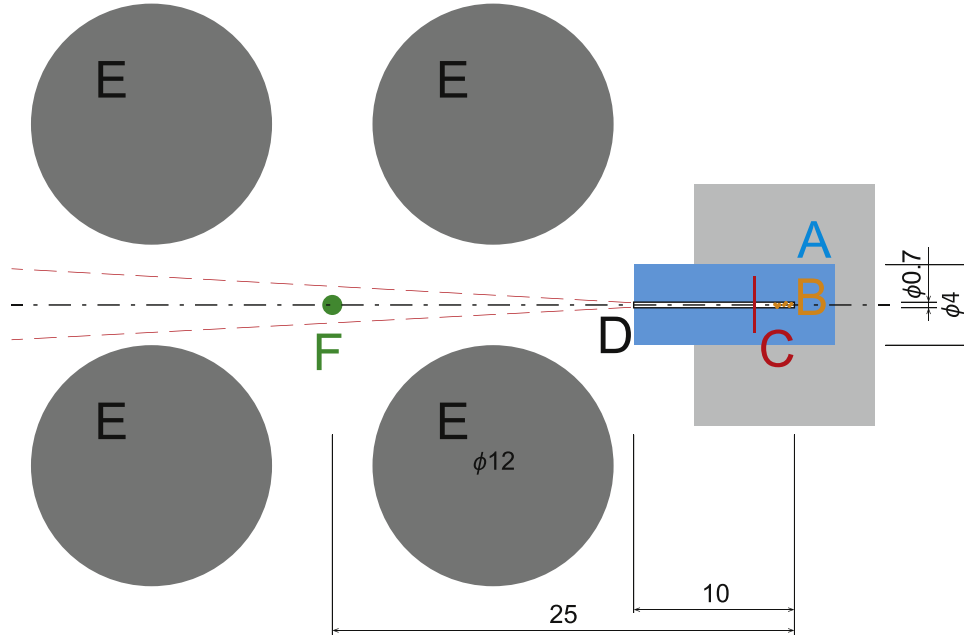


Figure 1. Schematic drawing of a positron source container. A: Pb cylinder with cavity; other parts of the container were made of stainless steel; a narrow hole was drilled in the container in order to compensate a pressure difference in the source cavity and the chamber. B: $^{22}\text{NaCl}$ salt deposited as water solution and dried before sealing. C: Kapton[®] foil (cylinder cavity closure). D: aperture. E: rod-shaped electrodes of the trap (cross section). F: tested grain. Only the most important dimensions (in millimeters) are given.

panels reveals that the charging rate increases with the grain size. In order to compare these histograms with the exponential distribution, the measured cumulative histograms were normalized to the unit area (left-hand scales). The distribution function of the exponential distribution, $F(\Delta t)$, with the expected value, τ , reads as

$$F(\Delta t) = 1 - \exp\left(-\frac{\Delta t}{\tau}\right). \quad (6)$$

The values of τ for various grains were obtained by a fit of Equation (6) to experimental data. The best fits are plotted in Figure 4 by solid red lines, and the values of τ which resulted in the best agreement of the exponential distribution $F(\Delta t)$ with experimental data are listed in Table 1. These values can be compared with the mean time between positron annihilation events, f_{annih}^{-1} , predicted by Equation (5). Since the whole measurements were run for more than a year, it was necessary to take into account a decay of the ^{22}Na radioisotope (note that the half-life time, $t_{1/2}$, is 2.6 yr), and thus the experimental values of τ have been corrected for the radioisotope decay:

$$\tau^* = \tau \cdot \exp\left(\frac{-t \ln 2}{t_{1/2}}\right), \quad (7)$$

where t is the time measured from the beginning of the experiment. We can conclude that the mean times, τ^* , between charging events corrected for a ^{22}Na decay and collected in Table 1 are in a very reasonable agreement (taking into account the experimental uncertainty) with the mean time between positron annihilation events, f_{annih}^{-1} , predicted by Equation (5), i.e., $\tau^* \approx f_{\text{annih}}^{-1}$. This supports the idea that the observed charging events come predominantly from positron annihilations inside grains.

From Equations (2)–(5) one can deduce that the ratio of the mean annihilation rates for spherical grains with diameters, d_1 and d_2 , and densities, ρ_1 and ρ_2 , would be proportional to the ratio of their masses, m_1 and m_2 :

$$\frac{\tau_2}{\tau_1} \approx \frac{f_{\text{annih},1}}{f_{\text{annih},2}} \approx \frac{m_1}{m_2}. \quad (8)$$

The mean rates between charging events measured for various grains are plotted as a function of the grain mass in Figure 5. The open circles show measured data, the full symbols stand for the average rates $(\tau^*)^{-1}$ between charging events corrected for a decay of the ^{22}Na positron source. One can see that the average rates corrected for ^{22}Na decay are directly proportional to the mass of dust grains, in accordance with Equation (8). This is consistent with the expectation that charging events are caused predominantly by positron annihilations inside grains.

Histograms of observed charge steps, Δq , for G_1 – G_4 are plotted in Figures 6(a)–(d), respectively. As was already noted, we attribute a few negative charging steps $\Delta q = -1$ e to parasitic low-energy secondary electrons created in the chamber. Thus, only positive charge steps are considered in the following analysis. The positron annihilation increases the grain charge by $+1$ e since one electron is removed by annihilation. Figure 6 demonstrates that the majority of measured events exhibits a charge step $\Delta q = +1$ e. However, charge steps larger than $+1$ e were detected, as well, and we associate them with inelastic collisions of a fast positron with electrons resulting in ionization when the transferred energy is higher than the binding energy of the electron. Since positrons and electrons have the same mass and the excitation energy is small in comparison with a typical positron energy, let us assume that a half of the positron kinetic energy is transferred to the electron in such a collision. As shown in Figure 2, positrons with kinetic energy up to ≈ 10 keV are stopped inside the micrometer-sized grain and so that they accelerate electrons

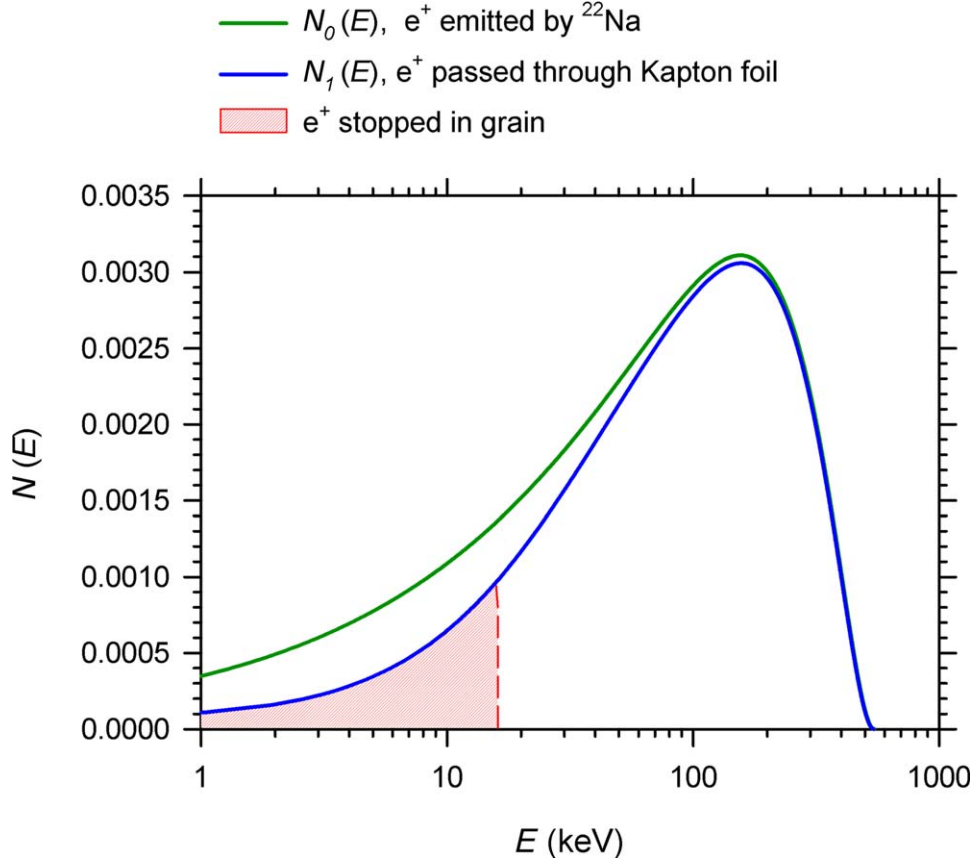


Figure 2. The energy spectrum of positrons emitted by a ^{22}Na radioisotope, $N_0(E)$ (green line); area of the spectrum is normalized to unity. The energy spectrum, $N_1(E)$, of positrons passed through $12\ \mu\text{m}$ thick Kapton[®] foil covering the source (blue line); area of the spectrum corresponds to the probability that a positron emitted by the ^{22}Na source penetrates through the Kapton[®] foil; a range of energies of positrons stopped in the grain G_4 is indicated by the hatched red area.

to energies $\approx 5\ \text{keV}$. The continuous slowing down approximation (CSDA) predicts the range of such electrons as $\approx 0.5\ \mu\text{m}$ and these electrons thus either remain inside the grain or they may escape. The latter effect results in an additional charging $+1\ e$ per each electron escaping from the grain. These electrons cause additional charging $+N_{\text{se}}\ e$, where N_{se} is the number of escaped secondary electrons. Thus, positron stopping and annihilation inside the grain result in a change of the grain charge $\Delta q = (N_{\text{se}} + 1)e$.

The quantity N_{se} can be obtained by subtracting $1\ e$ from the measured positive charge step expressed in the units of elementary charge. Histograms of observed charge steps with one elementary charge subtracted for G_1 – G_4 are plotted in Figures 7(a)–(d). Since escape of secondary electrons from the grain is a stochastic process with a certain time-independent probability, the number of escaped electrons, N_{se} , is a random variable which can be described by the Poisson distribution. The expected number of charge steps with height $\Delta q = (k + 1)e$, corresponding to the emission of $N_{\text{se}} = k$ electrons, is

$$N_k = N_{\text{tot}}^+ P(k|v), \quad (9)$$

where N_{tot}^+ is the total number of observed positive charging events and the probability $P(k|v)$ is given by the Poisson distribution:

$$P(k|v) = \frac{v^k e^{-v}}{k!}. \quad (10)$$

An estimator of the expected value of a Poisson distribution can be calculated from the measured data as

$$\hat{v} = \frac{\sum_k k N_k}{N_{\text{tot}}^+}. \quad (11)$$

Figure 7 shows that histograms of observed charging steps minus one elementary charge ($-1\ e$) can be well described by the Poisson distribution with an expected value given by Equation (11). This value for larger grains G_2 – G_4 is $\hat{v} \approx 0.6$. The expected value for the smallest grain G_1 is higher, $\hat{v} = 1.0 \pm 0.2$.

A secondary electron can be created anywhere inside a grain but it can escape from the grain only when it is located sufficiently close to the grain surface. Assuming that a secondary electron can escape from the grain only if it is created in a subsurface layer with certain thickness, δ , the escape probability is proportional to the volume fraction of such subsurface region:

$$P_{\text{escape}} \approx \frac{4\pi(d/2)^2\delta}{\frac{4}{3}\pi(d/2)^3} = 6\frac{\delta}{d}. \quad (12)$$

Note that the average number of secondary electrons created in the grain during positron slowing down depends on the difference between the initial and final positron energy. For larger grains the secondary electrons are spread in a larger volume and the probability that they fall into the subsurface

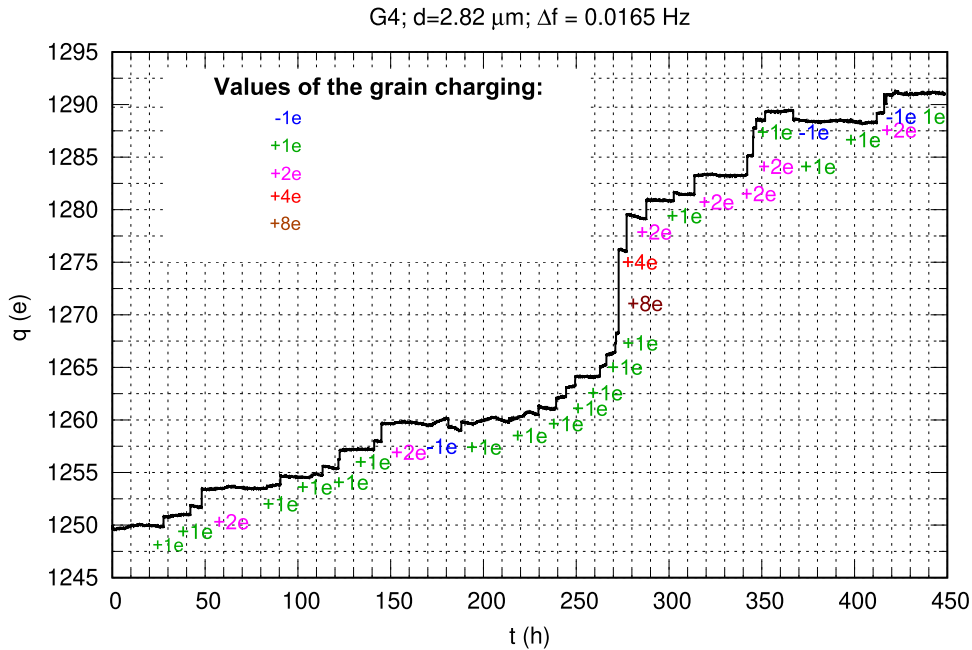


Figure 3. The example of the first 450 hours from the G_4 grain charging record. The step changes in the frequency correspond to the changes in one elementary charge and/or by its multiples. The change about one elementary charge is equivalent to a change of the grain oscillation frequency of about 0.0165 Hz .

layer is lower. As a consequence, the probability of electron escape decreases with increasing grain size.

Since P_{escape} scales inversely with the grain size d , the highest number of escaped secondary electrons would be observed for the smallest grain G_1 . Figure 8 shows the estimated average number of escaped secondary electrons, $\hat{\nu}$, as a function of the grain size d , and confirms this expectation. Although the uncertainties of the estimated $\hat{\nu}$ values are rather large, one can conclude that experimental data are in a reasonable accord with the dashed line computed by Equation (12) for the thickness of the subsurface layer $\delta \cong 0.2 \mu\text{m}$.

5. Discussion

We have demonstrated that the interaction of energetic positrons with silicate dust grains leads to their charging toward more positive values. The process can be described in the frame of the present theories of the positron interaction with solids if the dimensions of the grains are taken into account. This interaction results in charging of the isolated dust grain by two effects: (i) positron annihilation, and (ii) emission of secondary electrons excited inside the grain by the interaction of the grain electrons with positron.

A majority of the positrons emitted by a ^{22}Na radioisotope has energies in the order of $\approx 100 \text{ keV}$ (note that the mean energy of positrons emitted by ^{22}Na is 204 keV). The mean free path of such energetic positrons is one order of magnitude higher than the size of investigated grains and almost all these energetic positrons pass through the grain without any interaction, and thus mainly positrons from a low-energy part of β^+ energy spectra would interact at mesoscopic grains (Figure 2). We can conclude that observed charging events occurring inside mesoscopic grains are predominantly caused by slowing down and subsequent annihilation of positrons from a low-energy part of the β^+ spectrum with initial energies of the order of $\approx 10 \text{ keV}$. On the other hand, Figure 7 shows an excess

of events that were attributed to positron annihilation ($\Delta q - 1 = 0$) in comparison with the prediction given by Equation (12) for all grains. One can speculate whether this excess can be connected with positrons that emitted one electron and left the grain because such events cannot be distinguished experimentally from positron annihilation. These events (if they exist) would have also a Poisson distribution shifted by unity with respect to events accompanied with annihilation. We have tried to fit the data with the sum of two Poisson distributions, but the goodness of such a fit was similar to the fit shown in the Figure 7. Since the fit with the sum of two distributions has more free parameters and results in the same agreement with experiment, we may conclude that the simpler model with one Poisson distribution is sufficient and annihilation is likely a dominant source of $+1 e$ events.

6. Possible Consequences for Charging of Interstellar Dark Clouds

Interstellar “cold” dust clouds, the so-called IDCs, are objects consisting of myriads of mesoscopic grains with temperatures up to $10\text{--}50 \text{ K}$ (Men’shchikov et al. 1999; Tafalla et al. 2004; Etxaluze et al. 2011; Köhler et al. 2014; Dewangan et al. 2016). A substantial fraction of dust grains in IDCs is represented by silicate grains (Draine 2003). IDCs are bombarded by CR, consisting of photons of different energies, and corpuscular radiation, mainly electrons, positrons, and protons. It has to be mentioned that present models of the charging of IDCs are based on two main processes (Draine 1978; Ivlev et al. 2015; Ibáñez-Mejía et al. 2019):

1. Photoelectric emission caused predominantly by the interaction of UV photons emitted due to CR-induced H_2 fluorescence (Ivlev et al. 2015) with dust grains resulting in their positive charging.
2. A collection of low-energy electrons by dust grains leading to negative charging.

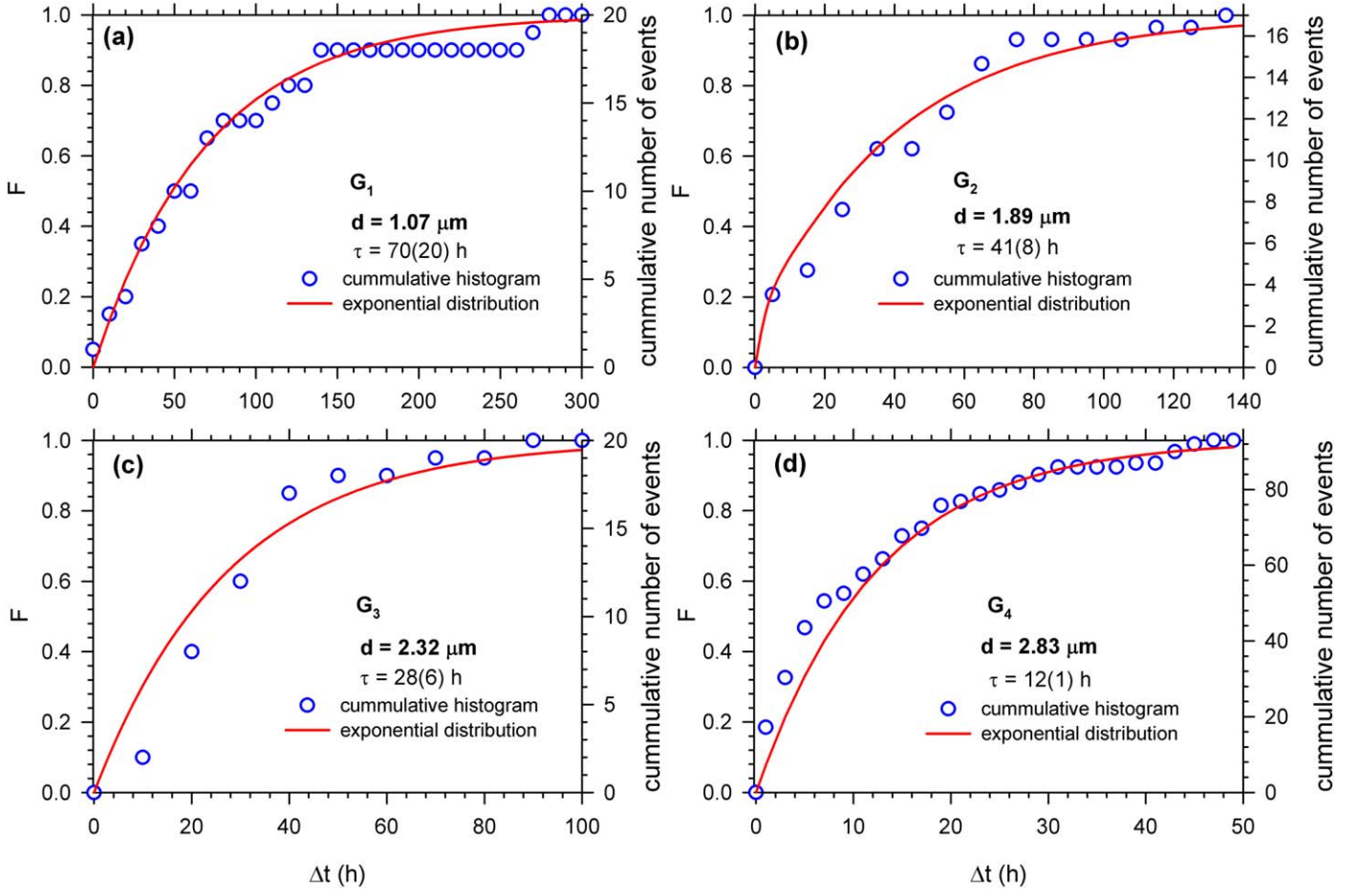


Figure 4. Cumulative (right-hand scales) and normalized cumulative (left-hand scales) histograms, respectively, of time intervals, Δt , between detected charging events for grains (a) G_1 , (b) G_2 , (c) G_3 , and (d) G_4 . The diameters, d , of the grains are given inside the panels. The red solid line shows the exponential distribution function, $F(\Delta t)$, with the expected value τ which is in the best agreement with the experiment.

The balance of these two processes can create an approximately equal population of positively and negatively charged grains, providing optimum conditions for coagulations of dust grains (Ivlev et al. 2015). On the other hand, the interaction of corpuscular radiation with dust grains could be more complex. We will mention positrons first.

A positron with an initial kinetic energy, $E_i < 1$ MeV, corresponding to energies emitted by β_+ radioisotopes, passing through an IDC gradually loses its energy by two main processes: (a) interaction with dust grains, and (b) inelastic scattering (ionization) of gas molecules, in particular H_2 , representing the most abundant chemical species in IDCs (Men'shchikov et al. 1999; Etxaluze et al. 2011).

The average distance traveled by a positron with initial energy E_i passing through an IDC and losing its energy so that it decreases to E_f can be calculated with CSDA as

$$R = \int_{E_f}^{E_i} \frac{dE}{P_G S_G(E) + (1 - P_G) S_{\text{ion}}(E)}, \quad (13)$$

where S_G is the stopping power given by Equation (2) and describes the energy loss of the positron due to interactions with dust grains. The quantity P_G in Equation (13) expresses the probability that a positron is located inside a dust grain, i.e., it loses its kinetic energy by interaction with electrons inside the grain, while $1 - P_G$ is the probability that a positron is not inside a grain, i.e., it loses its kinetic energy by interactions

with gas molecules. Assuming that the number density of dust grains is $\langle n_G \rangle$ and the grain diameter is d , the volume of a sphere containing on average single grain is $1/\langle n_G \rangle$. Hence, the probability that a positron flying through an IDC is inside a grain is given by the ratio of the grain volume and the volume of a sphere containing a single grain:

$$P_G = \frac{\pi}{6} d^3 \langle n_G \rangle. \quad (14)$$

The energy losses due to ionization of gas molecules are described by the Bethe-Bloch formula (Sigmund 2006):

$$S_{\text{ion}} = \frac{4\pi}{mc^2} Z n_{\text{gas}} \frac{1}{\beta^2} \left(\frac{e^2}{4\pi\epsilon_0} \right)^2 \left[\ln \left(\frac{2mc^2\beta^2}{I(1-\beta^2)} \right) - \beta^2 \right], \quad (15)$$

where m is the rest positron mass, c is the speed of light, $\beta = v/c$, v is the positron speed, Z is the proton number of molecules (for H_2 molecule $Z=2$), e is the elementary charge, ϵ_0 is the permittivity of vacuum, and I is the mean excitation energy of the target molecules, $I = 18.9$ eV (for a H_2 molecule; Wilson & Kamaratos 1981).

One can assume that a positron is stopped (thermalized) when its final energy falls down to $E_f \approx 0.01$ eV. A positron thermalized inside a dust grain is annihilated in the grain where it was stopped. It leads to positive charging of the grain as proved by our laboratory experiment. Note that the importance

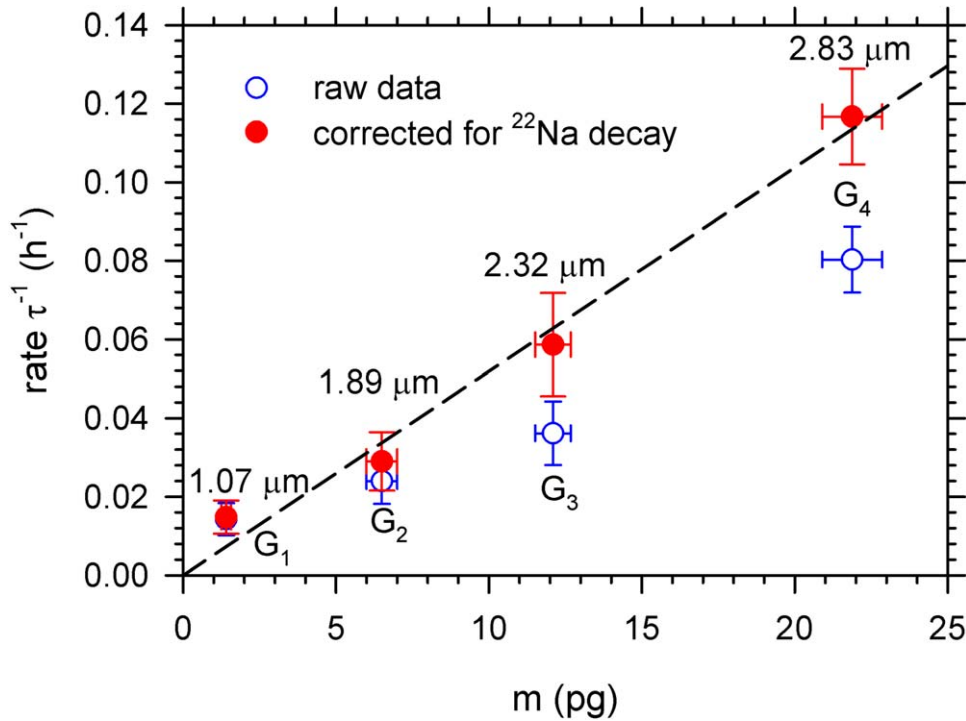


Figure 5. The average rates between charging events, τ^{-1} , measured for grains G_1 – G_4 plotted as a function of the grain mass, m . In order to compare results for the same activity of the positron source, the measured rates, τ^{-1} , plotted by open symbols, are corrected for the decay of the ^{22}Na source and corrected rates, $(\tau^*)^{-1}$, are plotted by red full symbols.

of positron annihilations in dust grains has been pointed out already in a pioneering work (Zurek 1985). Modeling of the shape of a 511 keV photopeak produced by annihilation gamma rays in the Galaxy and detected by INTEGRAL/SPI (Knödlseider et al. 2005) was performed by Guessoum et al. (2005). The modeling revealed that positron annihilations inside dust grains represent a dominating contribution to the 511 keV line in the hot-phase interstellar matter (Guessoum et al. 2005). The contribution of positron annihilations in dust grains in the cold-phase interstellar matter is uncertain and may fall into a range from 0% to 23% (Jean et al. 2006).

It should be mentioned that in the late stage of thermalization, when positron energy falls below ~ 100 eV, it may pick up an electron from a gas molecule and form positronium (Ps), a hydrogen-like bound state of an electron and positron (Mogensen 1995). The threshold energy of Ps formation in-flight is given by the ionization potential of a corresponding atom or molecule with a subtracted Ps formation energy of 6.8 eV (Mogensen 1995). The formation of Ps in-flight occurs in neutral gas media, while ionization of gas molecules strongly suppresses Ps formation (Murphy et al. 2005). Importantly, Ps formation in-flight leads to ionization (positive charging) of gas molecules due to removal of an electron picked up by Ps. This electron is subsequently destroyed by Ps self-annihilation.

Note that a thermalized positron may annihilate also by other processes, namely charge exchange with H, He, and H_2 (Guessoum et al. 2005), radiative recombination (Crannell et al. 1976; Gould 1989), or direct annihilation (Crannell et al. 1976; Bussard et al. 1979) with free electrons. The charge exchange with gas atoms and molecules has a threshold energy in the order of several eV (Guessoum et al. 2005). As a consequence, this process cannot occur in cold IDCs and appears only at high temperatures of thousands of kelvin (Prantzos et al. 2011). The cross sections for radiative recombinations and direct

annihilations with free electrons are very small (Crannell et al. 1976; Bussard et al. 1979; Gould 1989); for direct annihilation with electrons bound in gas atoms and molecules they are even smaller (Armour et al. 1990; Igarashi et al. 2002).

Hence, annihilation of positrons thermalized in dust grains and self-annihilation of Ps formed in-flight by pick up of an electron from gas molecules represent the most important processes of positron annihilation in IDCs. Since these processes occur preferentially in the outer regions of IDCs where the interaction of positrons from incoming CR takes place predominantly, one can introduce the characteristic parameter lining ratio (LRA) as the ratio of the thickness of the affected IDC edge, R , to the typical size, T , of the whole cloud, $\text{LRA} = R/T$. We should note that the LRA value represents the relative thickness of the layer affected by positrons of a given energy.

As an example of positron interaction with a real object, we can consider the results of analysis of the dust and gas molecules in the circumnuclear disk in the Galactic center (Etxaluze et al. 2011). In the cold region (24 K) of the disk, the particle density of H_2 molecules is $\langle n_{\text{H}_2} \rangle = 2.4 \times 10^4 \text{ cm}^{-3}$; the density of dust is $8.0 \times 10^{-22} \text{ g cm}^{-3}$; the mean dust grain size is $d \approx 0.1 \mu\text{m}$; and the material density of the grains is $\rho \approx 2.5 \text{ g cm}^{-3}$ (Etxaluze et al. 2011). Using these data as an input, we obtain the dust grain number density $\langle n_G \rangle = 6.1 \times 10^{-7} \text{ cm}^{-3}$. Examples of kinetic energy loss curves calculated using Equation (13) for positrons from CR with various initial energies passing through the disk’s cold region are plotted in Figure 9(a). For example, the CSDA range of 100 keV positrons in the circumnuclear disk is $R = 5.6 \times 10^3 \text{ au}$. Considering the estimated size of the cold area of the disk $T = 1.7 \times 10^5 \text{ au}$, one can determine its lining ratio $\text{LRA}_{\text{Sgr}} \approx 0.03$.

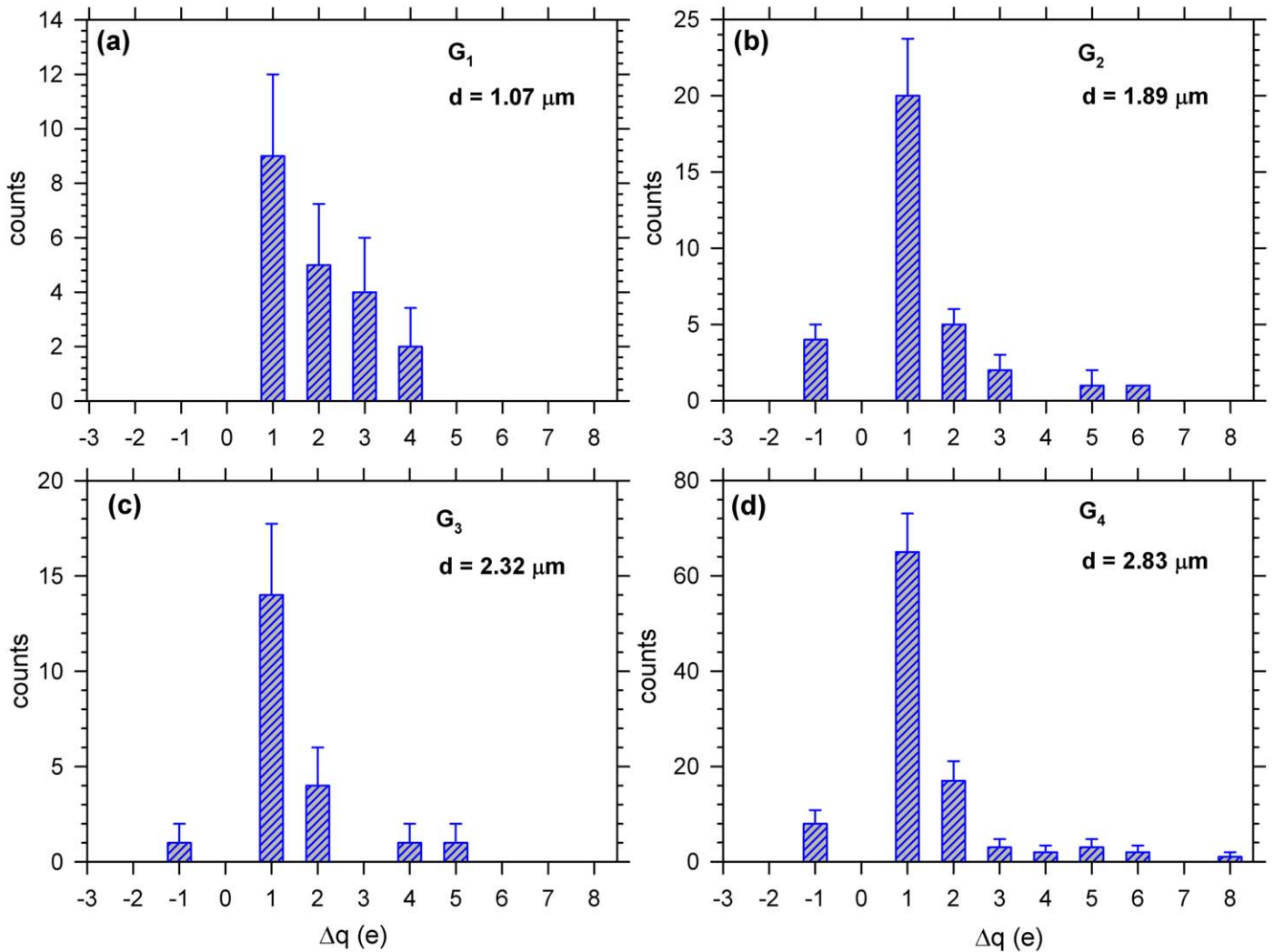


Figure 6. Histograms of measured charge steps, Δq , expressed in units of the elementary charge (+1 e) for grains (a) G_1 , (b) G_2 , (c) G_3 , and (d) G_4 .

As a second example, we discuss the dusty torus around HL Tauri (Men'shchikov et al. 1999) with a thickness of the outer cold area (10 K) $T_{\text{Tau}} \approx 10^4$ au. According to a self-consistent model of HL Tauri (Men'shchikov et al. 1999), in the very dense inner torus of HL Tauri the gas density decreases with radial distance, r , from the center as $\langle n_G \rangle \propto r^{-1.25}$. At $r \approx 90$ au from the center the slope of the density profile smoothly changes into $\langle n_G \rangle \propto r^{-2}$. Finally, in the outer region of HL Tauri the H_2 gas density approaches $\langle n_{\text{H}_2} \rangle \approx 6 \times 10^3 \text{ cm}^{-3}$ (Men'shchikov et al. 1999). The H_2 gas density profile is shown in Figure 9(b) by the red dashed line. Assuming a gas-to-dust mass ratio of 0.01 and a mean grain size $d \approx 1 \mu\text{m}$ (material density about 2.3 g cm^{-3}) (Men'shchikov et al. 1999), one can calculate using Equation (13) energy loss curves for positrons with various initial energies. The calculated energy loss curves are plotted in Figure 9(b) by solid lines. For example, the CSDA range of 100 keV positrons penetrating into HL Tauri is $R = 3.1 \times 10^3$ au and the lining ratio is $\text{LRA}_{\text{Tau}} \approx 0.3$, i.e., an order of magnitude larger than that for the circumnuclear disk in the Galactic center.

The results of the present experiment demonstrate that the interaction of positrons with dust grains leads to charging of these grains with a positive charge that is often larger than +1 e. We can expect that a positron during its slowing down interacts

on average with $1/6\pi d^2 \langle n_G \rangle R(E_i)$ grains. If the average number of emitted secondary electrons per grain positron interacted with is ν , then the average number of secondary electrons emitted during the positron slowing down is

$$N_{\text{se}} = \frac{1}{6} \pi \nu d^2 \langle n_G \rangle R(E_i). \quad (16)$$

Considering that the secondary electrons emitted from grains are mostly collected in other grains, there is no overall charging. However, a fraction of secondary electrons originating in the vicinity of the IDC's edge may escape from the cloud into free space. The thickness of such a region is approximately inversely proportional to the product of the dust grain number density and the cross section for electron interaction in the grain. Quantitatively considering positrons with an energy of ≈ 100 keV, one can expect production of secondary electrons with energies in the order of ~ 50 keV. The CSDA range of such electrons can be calculated using Equation (13) with the stopping power S_G for electrons (Batra & Sehgal 1970). This yielded CSDA ranges of 1.5×10^3 and 1.7×10^2 au in the dust circumnuclear disk in the Galactic center and in the HL Tauri dusty torus, respectively.

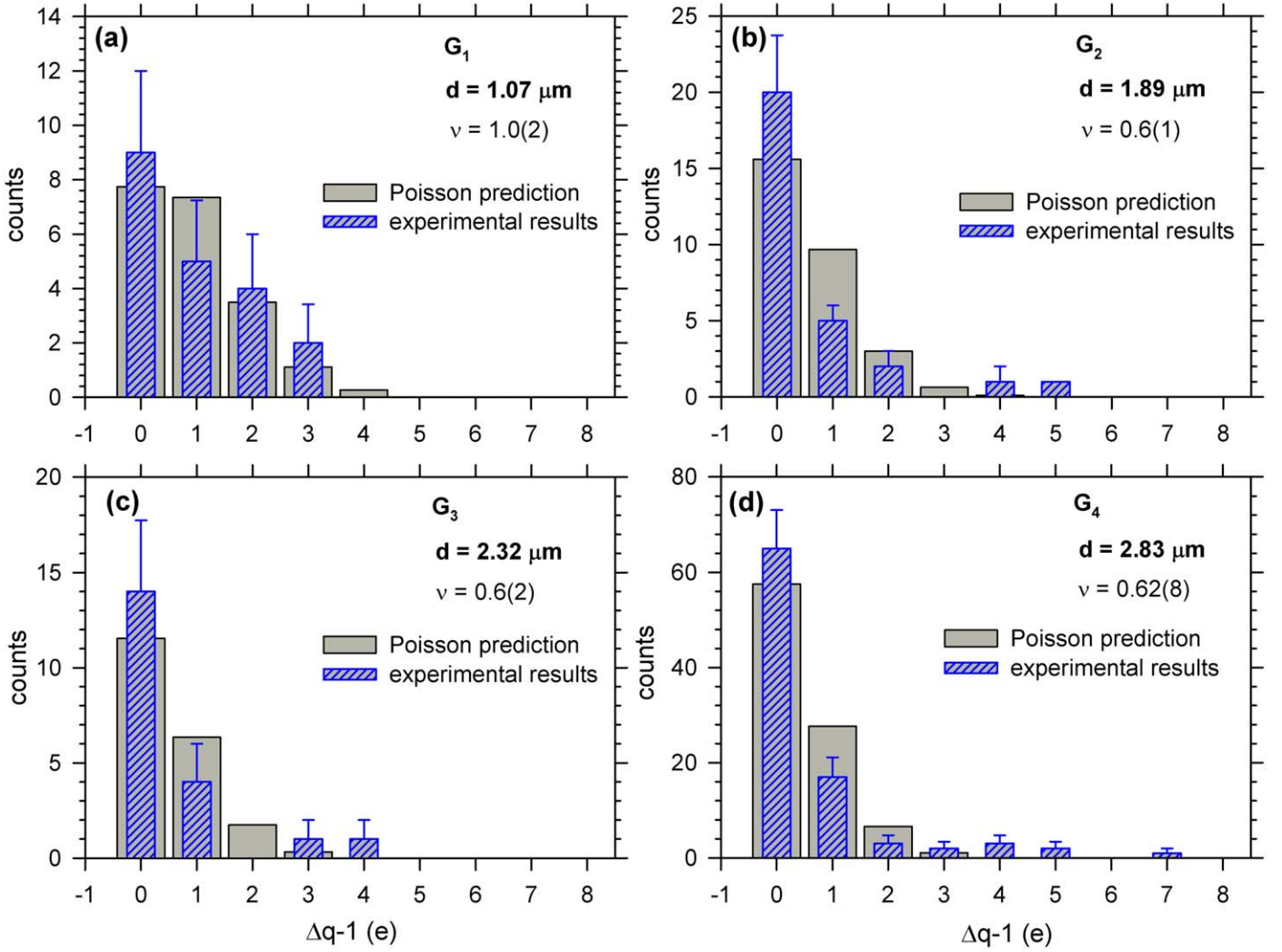


Figure 7. Histograms of measured charge steps, Δq , expressed in the units of elementary charge (e) minus 1 (hatched columns) for (a) G_1 , (b) G_2 , (c) G_3 , and (d) G_4 . Grey columns show prediction of the Poisson distribution with the expected value v .

Note that electrons released from gas atoms and molecules due to inelastic scattering with positrons during their slowing down have energies in the order of tens of eV and are, therefore, collected in dust grains or positively charged ions of gas molecules. These electrons, therefore, do not contribute to charging of the IDC. On the other hand, in-flight formation of Ps leaves gas molecules in a +1 e charged state, and this charge is not compensated for since picked up electrons disappear during Ps self-annihilation. Hence, in-flight formation of Ps during positron interaction with gas molecules also contributes to positive charging of IDCs in addition to positron annihilations inside dust grains.

Now we compare the estimated charging rate of an IDC caused by positron interaction and the charging rate due to H_2 fluorescence UV-radiation-induced photoemission. The flux, F_{UV} , of UV photons in the energy range of 11.2–13.6 eV corresponding to H_2 fluorescence can be estimated as (Ivlev et al. 2015)

$$F_{UV} [\text{cm}^{-2}\text{s}^{-1}] \approx 960 \left(\frac{1}{1 - \omega} \right) \left(\frac{\xi}{10^{-17} \text{ s}^{-1}} \right) \times \left(\frac{N(\text{H}_2)/A_V}{10^{21} \text{ cm}^{-2} \text{ mag}^{-1}} \right) \left(\frac{R_V}{3.2} \right)^{1.5}, \quad (17)$$

where ξ is the CR ionization rate, $\omega = 0.5$ is the dust albedo at the UV wavelength range, $R_V = 3.1$ is a measure of the slope of the extinction at visible wavelengths (Ceccchi-Pestellini & Aiello 1992; Draine 2011), and the gas-to-extinction ratio $N(\text{H}_2)/A_V = 1.87 \times 10^{21} \text{ cm}^{-2} \text{ mag}^{-1}$ (Ibáñez-Mejía et al. 2019). Using the CR ionization rate $\xi = 6 \times 10^{-17} \text{ s}^{-1}$, corresponding to the outer region of the IDC (Ivlev et al. 2015), we get a UV photon flux $F_{UV} \approx 2 \times 10^4 \text{ photons s}^{-1}$. The photoemission flux, J_{PE} , is approximately given by the expression (Ivlev et al. 2015)

$$J_{PE} \approx \pi d^2 F_{UV} \langle Y(\nu) Q_{\text{abs}}(\nu) \rangle_{UV}, \quad (18)$$

where $\langle Y(\nu) Q_{\text{abs}}(\nu) \rangle_{UV} = 0.2$ (Weingartner et al. 2006) is the product of the photoemission yield, $Y(\nu)$, and the absorption efficiency, $Q_{\text{abs}}(\nu)$, averaged over the Lyman and Werner bands for a grain size $d = 0.1 \mu\text{m}$. Equation (18) yields the photoemission flux $J_{PE} \approx 1.3 \times 10^{-6} \text{ s}^{-1}$.

A rough estimation of the positron annihilation rate per grain is given by the expression (Prantzos et al. 2011)

$$J_{G,\text{annih}} \approx \langle n_G \rangle \frac{\pi}{4} d^2 v, \quad (19)$$

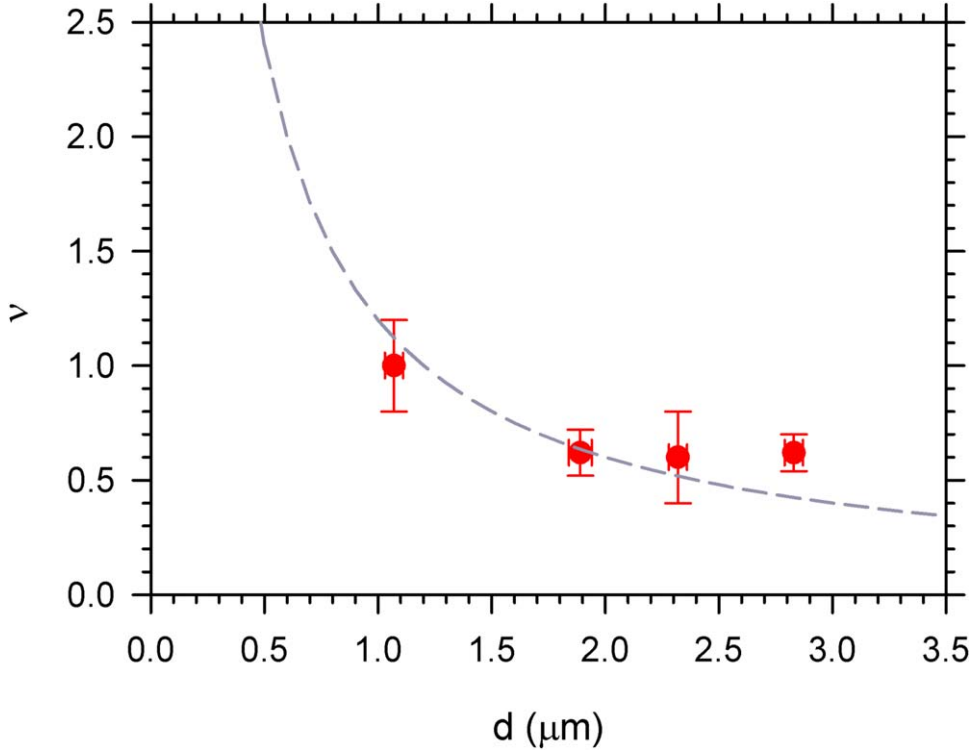


Figure 8. The estimated average number of escaped secondary electrons, ν , as a function of the grain size, d . The dashed line shows the relation predicted by Equation (12) with the thickness of the subsurface layer $\delta = 0.2 \mu\text{m}$.

where $v = \sqrt{2E/m}$ is the positron speed in the late stage of thermalization. Using $v \approx 0.06c$, corresponding to the positron energy $E \approx 1 \text{ keV}$, as a typical value in the late stage of thermalization, and assuming a typical particle density in the circumnuclear disk in the Galactic center ($\langle n_G \rangle \approx 6 \times 10^{-7} \text{ cm}^{-3}$ (see Figure 9(a)), and a grain diameter $d = 0.1 \mu\text{m}$ (Etzaluze et al. 2011), one obtains $J_{G,\text{annih}} \approx 10^{-11} \text{ s}^{-1}$. This value is five orders of magnitude lower than the photoemission charging rate J_{PE} , indicating that positive charging of grains caused by photoemission is clearly a dominating process.

One has to consider also positron-induced positive charging of IDCs caused by in-flight Ps formation in the course of positron thermalization. Ps picks up an electron from a gas molecule leading to its ionization (+1 e charging). Since the picked up electron is removed by Ps self-annihilation, the charge neutrality in the IDC is not balanced and positive charging occurs. In analogy to Equation (19), the charging rate due to Ps formation in-flight can be estimated from the expression (Prantzos et al. 2011)

$$J_{Ps,\text{annih}} \approx \langle n_{\text{H}_2} \rangle \sigma v. \quad (20)$$

Using the average H_2 gas density in the circumnuclear disk in the Galactic center ($\langle n_{\text{H}_2} \rangle \approx 2.4 \times 10^4 \text{ cm}^{-3}$ (see Figure 9(b)), and a cross section for Ps formation in-flight $\sigma \approx 10^{-16} \text{ cm}^2$ (Guessoum et al. 2005), Equation (20) yields the Ps charging rate $J_{Ps,\text{annih}} \approx 5 \times 10^{-7} \text{ s}^{-1}$, which is comparable in the order of magnitude with J_{PE} . Hence, self-annihilation of Ps formed in-flight significantly contributes to positive charging of IDCs, and this process occurs preferentially in the IDC's edge.

It is known that positron annihilation produces two gamma quanta with an energy of 511 keV. These annihilation gamma rays penetrate into IDCs significantly deeper than positrons,

and they may interact with dust grains along their path through the IDC. This interaction results in positive charging of grains due to photoelectric emission or Compton scattering. However, it occurs in the deep interior of IDC and electrons emitted from a grain due to interaction with annihilation gamma rays are subsequently collected in some other grain so that the net charge of the IDC remains neutral.

The interaction of energetic electrons with an IDC would be almost similar with the exceptions of annihilation and Ps formation. An additional difference consists in the fact that the scattering cross section for electrons is higher than for positrons, and electrons have a higher probability of scattering to large angles (Valkealahti & Nieminen 1984). As a consequence, the CSDA range of electrons is smaller than that of positrons. The electron impact onto grains leads to emission of secondary electrons and some of them can have energies sufficient for escape from the IDC because, based on laboratory investigations of the charging of dust grains with energetic electrons (Pavlů et al. 2009), the secondary electrons can reach energies close to one half of the primary particle energy. This means that, similarly to positrons, impacts of energetic electrons would also lead to positive charging of the IDC edge. However, similarly to the positrons charging rate of a grain in the IDC due to electrons, is negligible compared to the photoemission flux due to UV radiation.

Positive ions regardless of their charge state would bring to an IDC their positive charge without any important consequence because the yield of ion-induced secondary emission is small compared to the case of electrons (Jerab et al. 2007; Pavlu et al. 2008). On the other hand, a probability of escape of secondary electrons generated by this process from IDC is relatively large because the ion range is significantly lower than that of positrons or electrons. As a consequence, the secondary

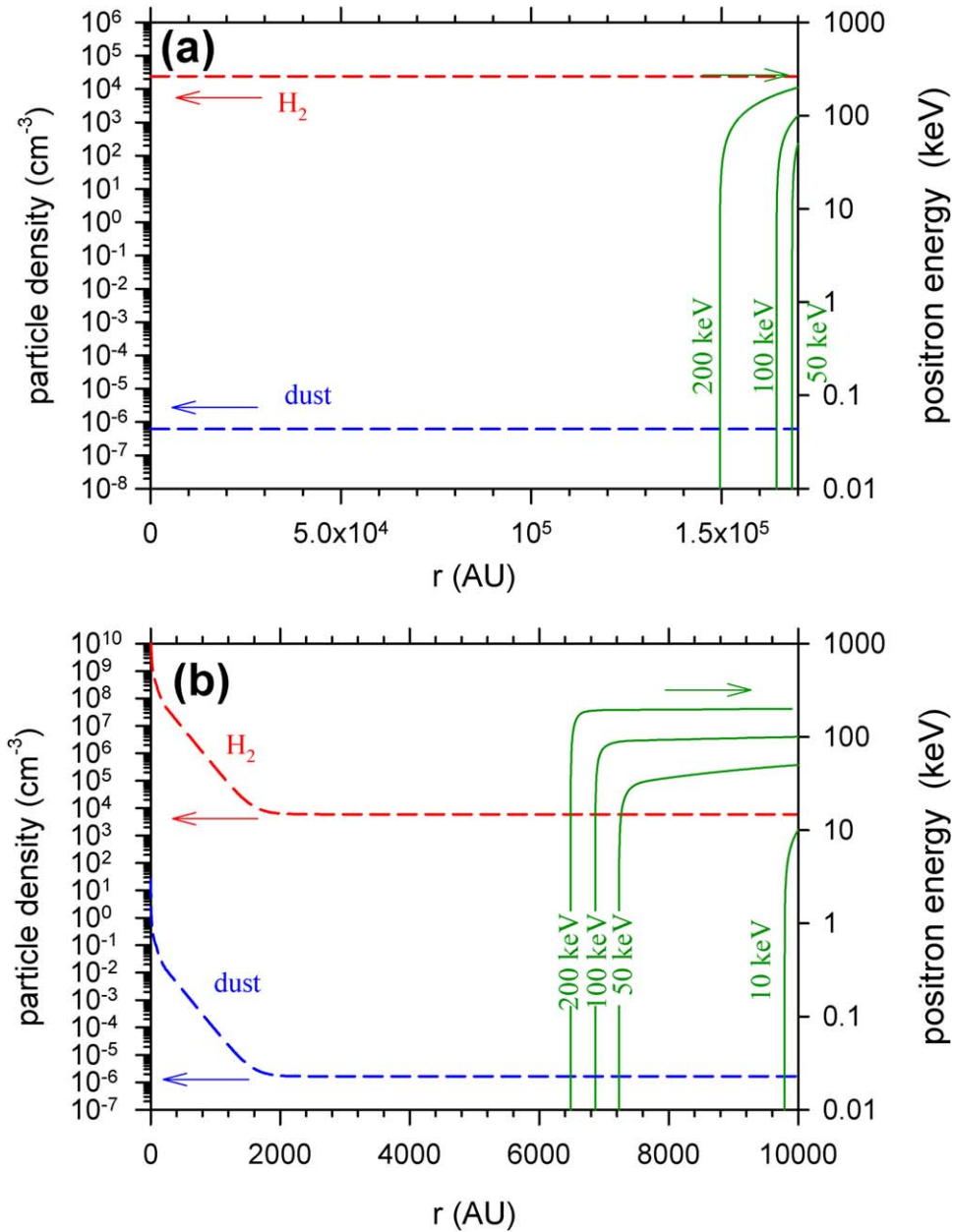


Figure 9. The radial dependence of the particle density of H_2 molecules and dust grains (dashed lines, left vertical axis) of (a) the cold region of the circumnuclear disk dust in the Galactic center region (Etaluzze et al. 2011), (b) HL Tauri dusty torus (Men’shchikov et al. 1999). The development of the kinetic energy of positrons entering the dust cloud with various initial kinetic energies of 200, 100, 50, and 10 keV is plotted in the figure, as well (green solid lines, right vertical axis). Note different horizontal length scales on the lower and upper panels.

electrons generated during ion slowing down would be generated close to the IDC edge. Such electrons would also increase the positive charging of the outer layer, although similarly to positrons and electrons the charging rate is negligible compared to that caused by UV-radiation-induced photoemission.

Coupling all the above discussed processes together, we can conclude that bombarding of an IDC with CR would lead to positive charging occurring preferentially in its outer edge. The most important charging process caused by impacted positrons seems to be self-annihilation of Ps formed in-flight during positron slowing down. The estimated charging rate of this process is comparable in the order of magnitude with that for photoemission caused by H_2 fluorescence UV radiation. In

addition, a fraction of secondary electrons produced during slowing down of incident CR electrons or positrons may escape from IDC dust, and this process also contributes to positive charging of the IDC edge. The positive charging of an IDC’s outer layers should be considered in models of IDC evolution.






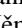
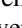
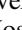
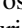
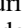
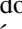
7. Conclusion

Positron-induced charging of mesoscopic SiO_2 grains caught in an electrodynamic quadrupole trap has been investigated in the present work. We have shown that positron annihilation results in $+1e$ charging due to disappearing electron and additional positive charging occurs due to the emitted secondary electrons created in the grain during positron

slowing down. The average rate of charging events observed in the experiment is in a good agreement with the prediction of a model based on the CSDA and assuming annihilation of thermalized positrons only. We discuss implications of the investigated processes to charging of interstellar dust clouds and we found that the charging rate due to annihilation of positrons in IDC dust grains is negligible compared to the charging rate due to photoemission caused predominantly by H₂ fluorescence UV radiation. However, interaction of positrons with gas molecules (mainly H₂) during the final stages of positron thermalization may result in pick up of an electron and in-flight formation of Ps. Since a picked up electron disappears by Ps self-annihilation, this process also contributes to positive charging of IDC. The estimated charging rate caused by the Ps self-annihilation is comparable in the order of magnitude with that for the UV-radiation-induced photoemission. Using particular examples of the dust circumnuclear disk in the Galactic center and dusty torus around HL Tauri, we showed that stopping of energetic positrons and their interaction with gas molecules result in positive charging of the edge of the dust cloud, while the net charge in the cloud interior remains neutral. (This concept inspired the motto of the article.)

This work was supported by the Czech Ministry of Education, Youth and Sport under contract LTAUSA17066 and the Czech Science Foundation, Project No. 20-13616Y. Computational resources were supplied by the project “e-Infrastruktura CZ” (e-INFRA LM2018140) provided within the program Projects of Large Research, Development and Innovations Infrastructures.

ORCID iDs

Jan Wild  <https://orcid.org/0000-0003-2216-2898>
 Jakub Čížek  <https://orcid.org/0000-0001-9961-8545>
 Libor Nouzák  <https://orcid.org/0000-0002-0485-210X>
 Jiří Pavlů  <https://orcid.org/0000-0003-3295-6501>
 Jana Šafránková  <https://orcid.org/0000-0003-4178-5206>
 Zdeněk Němeček  <https://orcid.org/0000-0002-8160-3051>
 Jakub Vaverka  <https://orcid.org/0000-0003-2177-0955>
 Dalibor Nosek  <https://orcid.org/0000-0001-6219-200X>
 Tomáš Burian  <https://orcid.org/0000-0003-3982-9978>
 Anna Wildová  <https://orcid.org/0000-0001-8739-4273>
 Jan Broulím  <https://orcid.org/0000-0003-4631-9933>

References

- Ackermann, M., Ajello, M., Allafort, A., et al. 2012, *PhRvL*, **108**, 011103
 Adriani, O., Barbarino, G. C., Bazilevskaya, G. A., et al. 2013a, *ApJ*, **765**, 91
 Adriani, O., Barbarino, G. C., Bazilevskaya, G. A., et al. 2013b, *PhRvL*, **111**, 081102
 Adriani, O., Barbarino, G. C., Bazilevskaya, G. A., et al. 2015, *ApJ*, **810**, 142
 Aguilar, M., Alberti, G., Alpat, B., et al. 2013, *PhRvL*, **110**, 141102
 Armour, E. A. G., Baker, D. J., & Plummer, M. 1990, *JPhB*, **23**, 3057
 Batra, R. K. 1987, *NIMPB*, **28**, 195
 Batra, R. K., & Sehgal, M. L. 1970, *NuPhA*, **156**, 314
 Beránek, M., Čermák, I., Němeček, Z., et al. 2012, *RSci*, **83**, 115109
 Brunger, M. J., Buckman, S. J., & Ratnavelu, K. 2017, *JPCRD*, **46**, 023102
 Bussard, R. W., Ramaty, R., & Drachman, R. J. 1979, *ApJ*, **228**, 928
 Cecchi-Pestellini, C., & Aiello, S. 1992, *MNRAS*, **258**, 125
 Charlton, M. 1985, *RPPH*, **48**, 737
 Crannell, C. J., Joyce, G., Ramaty, R., & Wertz, C. 1976, *ApJ*, **210**, 582
 Cummings, A. C., Stone, E. C., Heikkilä, B. C., et al. 2016, *ApJ*, **831**, 18
 Dewangan, L. K., Ojha, D. K., Zinchenko, I., et al. 2016, *ApJ*, **833**, 246
 Dirac, P. A. M. 1930, *MPCPS*, **26**, 361
 Draine, B. T. 1978, *ApJS*, **36**, 595
 Draine, B. T. 2003, *ARA&A*, **41**, 241
 Draine, B. T. 2011, *Physics of the Interstellar and Intergalactic Medium* (Princeton, NJ: Princeton Univ. Press)
 Etzaluze, M., Smith, H. A., Tolls, V., Stark, A. A., & González-Alfonso, E. 2011, *AJ*, **142**, 134
 Fermi, E. 1934, *ZPhy*, **88**, 161
 Fuller, G. M., Kusenko, A., Radice, D., & Takhistov, V. 2019, *PhRvL*, **122**, 121101
 Gould, R. J. 1989, *ApJ*, **344**, 232
 Groom, D. E., & Klein, S. R. 2000, *EPJC*, **15**, 163
 Guessoum, N., Jean, P., & Gillard, W. 2005, *A&A*, **436**, 171
 Guessoum, N., Jean, P., & Gillard, W. 2006, *ApSS*, **252**, 3352
 Gupta, S. K., Govil, J. C., Gupta, D. K., Tyagi, R. K., & Varma, O. P. 1982, *Int. J. Appl. Radiat. Isot.*, **33**, 773
 Huginschmidt, C. 2016, *SurSR*, **71**, 547
 Ibáñez-Mejía, J. C., Walch, S., Ivlev, A. V., et al. 2019, *MNRAS*, **485**, 1220
 Igarashi, A., Kimura, M., & Shimamura, I. 2002, *PhRvL*, **89**, 123201
 Ivlev, A. V., Padovani, M., Galli, D., & Caselli, P. 2015, *ApJ*, **812**, 135
 Jean, P., Knödseder, J., Gillard, W., et al. 2006, *A&A*, **445**, 579
 Jerab, M., Richterová, I., Pavlu, J., Safrankova, J., & Nemecek, Z. 2007, *ITPS*, **35**, 292
 Knödseder, J., Jean, P., Lonjou, V., et al. 2005, *A&A*, **441**, 513
 Köhler, M., Habart, E., Arab, H., et al. 2014, *A&A*, **569**, A109
 Krause-Rehberg, R., & Leipner, H. 1999, *Positron Annihilation in Semiconductors* (Berlin: Springer)
 Leo, W. R. 1987, *Techniques for Nuclear and Particle Physics Experiments* (Berlin: Springer)
 Men'shchikov, A. B., Henning, T., & Fischer, O. 1999, *ApJ*, **519**, 257
 Mogensen, O. 1995, *Positron Annihilation in Chemistry* (Berlin: Springer)
 Murphy, R. J., Share, G. H., Skibo, J. G., & Kozlovsky, B. 2005, *ApJS*, **161**, 495
 Nouzák, L., Richterová, I., Pavlů, J., Němeček, Z., & Šafránková, J. 2016, *ITPS*, **44**, 512
 Padovani, M., Ivlev, A. V., Galli, D., et al. 2020, *SSRv*, **29**, 216
 Pavlu, J., Richterová, I., Nemecek, Z., Safrankova, J., & Cermak, I. 2008, *FaDi*, **137**, 139
 Pavlů, J., Šafránková, J., Němeček, Z., & Richterová, I. 2009, *CoPP*, **49**, 169
 Pavlů, J., Velyhan, A., Richterová, I., et al. 2004, *ITPS*, **32**, 704
 Prantzos, N., Boehm, C., Bykov, A., et al. 2011, *RvMP*, **83**, 1001
 Puska, M. J., & Nieminen, R. M. 1994, *RvMP*, **66**, 841
 Renoud, R., Mady, F., Attard, C., Bigarré, J., & Ganachaud, J.-P. 2004, *PSSAR*, **201**, 2119
 Richterová, I., Beránek, M., Pavlů, J., Němeček, Z., & Šafránková, J. 2010, *PhRvB*, **81**, 075406
 Richterová, I., Pavlů, J., Němeček, Z., & Šafránková, J. 2006, *PhRvB*, **74**, 235430
 Schultz, P. J., & Lynn, K. G. 1988, *RvMP*, **60**, 701
 Sigmund, P. 2006, *Penetration and Radiation Effects*. Springer Series in Solid State Sciences (Berlin: Springer)
 Strong, A. W., Moskalenko, I. V., & Ptuskin, V. S. 2007, *ARNPS*, **57**, 285
 Strong, A. W., Orlando, E., & Jaffe, T. R. 2011, *A&A*, **534**, A54
 Svestka, J., Cermak, I., & Grün, E. 1993, *AdSpr*, **13**, 199
 Tafalla, M., Myers, P. C., Caselli, P., & Walmsley, C. M. 2004, *A&A*, **416**, 191
 Tsai, Y.-S. 1974, *RvMP*, **46**, 815
 Valkealahti, S., & Nieminen, R. M. 1984, *ApPhA*, **35**, 51
 van Dishoeck, E. F. 2014, *FaDi*, **168**, 9
 Weingartner, J. C., Draine, B. T., & Barr, D. K. 2006, *ApJ*, **645**, 1188
 Wilson, W., & Kamaratos, E. 1981, *PhLA*, **85**, 27
 Žilavý, P., Němeček, Z., & Šafránková, J. 1999, in *WDS'99 Proceedings of Contributed Papers: Part II—Physics of Plasmas and Ionized Media*, ed. J. Šafránková (Prague: Matfyzpress), 252
 Zurek, W. H. 1985, *ApJ*, **289**, 603